In situ optical monitoring of RDX nanoparticles formation during rapid expansion of supercritical CO_2 solutions†

Takuya Matsunaga,[a] Andrei V. Chernyshev,[b] Evgeni N. Chesnokov[b] and Lev N. Krasnoperov*[a]

Received 23rd May 2007, Accepted 9th July 2007
First published as an Advance Article on the web 21st August 2007
DOI: 10.1039/b707833c

Nanoparticles of RDX (cyclotrimethylenetrinitramine) generated by RESS (rapid expansion of supercritical solutions) using supercritical CO_2 were characterized *in situ* by a pulsed laser light scattering imaging technique using a gated ICCD (intensified CCD) camera. The absolute sensitivity calibration was performed using Rayleigh light scattering from air as well as light scattering from standard polystyrene spheres. The size distribution functions of the particles formed in the RESS jet were determined using the calibrated sensitivity. The diameter of RDX particles formed at the pre-expansion pressure of 180 bar was 73 nm at the maximum of the size distribution function. Assuming that the particles near the nozzle consisted mainly of CO_2 and the size distribution was log-normal, the diameter of the particles near the nozzle (7.5 mm from the nozzle) at the distribution maximum was 3.3 μm at the pre-expansion pressure of 180 bar. The number densities of the particles in the RESS jet were determined by counting individual particles in the light scattering images. Based on the measured particle size distributions and the number density of particles along the RESS jet, the mechanism of particle formation in RESS is discussed. The homogeneous nucleation mechanism is rejected as it fails to explain the large particle size experimentally observed. Instead, a modified "spray-drying" mechanism is suggested.

1. Introduction

Reduction of crystal size of energetic materials has been achieved using RESS (rapid expansion of supercritical solutions),[1–3] in order to decrease the impact sensitivity of the formulations based on these materials. The decrease in the sensitivity, which allows safe handling of energetic materials, with their reduced crystal size, was experimentally verified.[4] The RESS process is a common method to produce particles of submicron to micron size for materials which are soluble in a supercritical solvent.[5,6] For energetic materials this process is very attractive, given that physical methods (such as grinding) for nanoparticle production are usually prohibited due to their explosive nature.

Particle formation by RESS has been studied theoretically as well.[7–15] In several studies the particle size was calculated assuming the mechanism of homogeneous nucleation, however, the predictions were not consistent with the experimental results.[8,14] The particle size predicted by the homogeneous nucleation model was substantially smaller than that experimentally observed. Subsequent agglomeration was suggested as being responsible for the larger particle size.[14,15] Furthermore, it was pointed out,[16,17] that the particle coagulation might take place at the sample collection and, therefore, the size distribution of particles collected from RESS might largely depend on the sampling process. Therefore, the comparison between the theoretically predicted particle sizes and the experimental results such as from scanning electron microscopy (SEM) should be made with much caution. For this reason alternative experimental methods for the determination of the true size distribution functions of particles produced by RESS, that are free from sampling effects, are to be developed.

The particle size and the particle size distribution functions are often determined by SEM of the final powder samples. In this approach, however, uniform collection (*i.e.*, without the size discrimination) of particles from the RESS jet is questionable, because there could be difficulties in efficient collection of very small particles (below 100 nm in diameter). There are several techniques used for the *in situ* characterization of the RESS process such as the three-wavelength-extinction measurement (3-WEM),[8,15,16,18,19] Fourier transform infrared (FTIR) spectroscopy,[16,19] and the laser-based shadowgraphy (LABS).[18] In the 3-WEM technique the extinction of incident light as a result of the light scattering by the particles is measured using three different wavelengths. Then, the particle size and the particle number density are determined assuming a particular size distribution function. FTIR is a useful technique for investigating chemical compositions in RESS jet. Both 3-WEM and FTIR techniques rely upon the assumed size distribution functions. Moreover, light scattering by the

[a] *Department of Chemistry and Environmental Science, New Jersey Institute of Technology, University Heights, Newark, NJ 07102, USA. E-mail: Krasnoperov@adm.njit.edu; Fax: +1 973 596 3586*
[b] *Institute of Chemical Kinetics and Combustion, Institutskaya 3, 630090 Novosibirsk, Russia*

† Electronic supplementary information (ESI) available: Calibration of the sensitivity of the ICCD camera (Appendix A); evaluation of the index of refraction of polystyrene and RDX at 248 nm (Appendix B); the dilution by air entrainment estimated based on the temperature profile (Appendix C). See DOI: 10.1039/b707833c

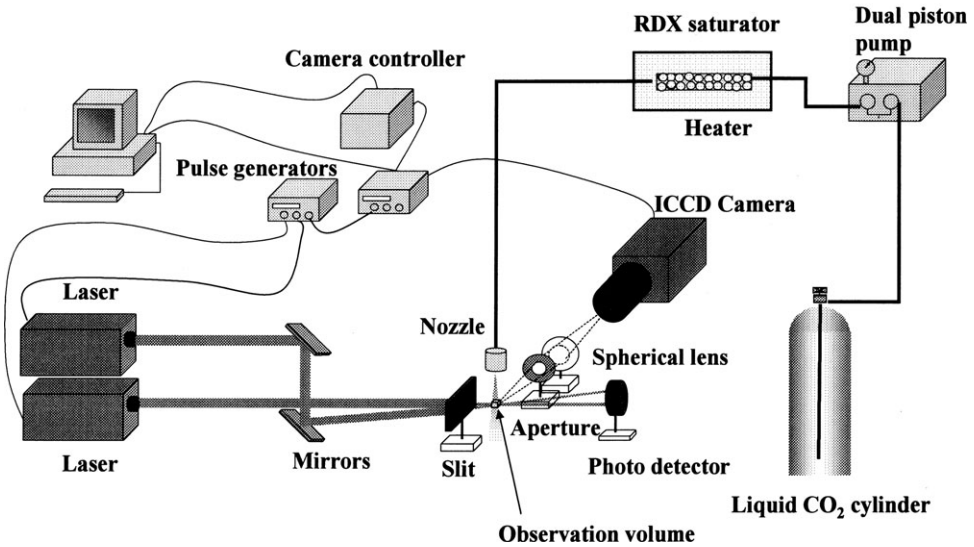

Fig. 1 Experimental setup.

turbulent flow in the RESS jet might interfere with the measurements. The LABS produces a magnified shadowgraph picture of individual particles. The particle size is determined by measuring the size of spots in the pictures. With this technique *in situ* characterization of large particles is possible, small particles (with the diameters less than the wavelength of the incident light) cannot be monitored.

In this research the laser light scattering imaging system coupled to a gated ICCD (intensified CCD) camera was used to capture images of individual particles in the ICCD frames. A large number of individual frames have been processed to recover the particles size distribution functions. In this approach each single spot corresponding to a particle was resolved and treated separately. One of the advantages of this particle-by-particle treatment is that it produces particle size distributions without assumptions on the shape of the distribution functions in the range of the sizes where the inverse Mie problem has unique solution (smaller than 106 nm for RDX particles). Another advantage is that in the images one can differentiate light scattering by the turbulent RESS flow from the scattering by the particles. The technique provides the number density of the particles and the particle size distribution in the RESS jet. Such information is important for establishing the mechanism of the particle formation in the RESS process.

The light scattering imaging system was calibrated using standard latex particles with known diameters as well as Rayleigh scattering from air to determine the absolute sensitivity. The scattering light intensity distribution functions from RDX particles formed by RESS were determined *in situ* at different distances from the expansion nozzle. The series of the intensity distribution functions were converted to the particle size distribution functions using the absolute sensitivity obtained in the calibrations based on Rayleigh and Mie theories.[20] Finally, the mechanism of particle formation process in the RESS is discussed based on the experimental results.

2. Experimental

The RESS system is schematically shown in Fig. 1. Liquid CO_2 (CD 3.0, Praxair Inc.) was taken from a cylinder and pumped up to a desired pressure by a high-pressure dual piston pump (Model P-50, Thar Design Inc.). Then it was heated to a supercritical extraction temperature and flowed through a saturator loaded with glass beads of 3 mm in diameter coated by RDX. The saturated supercritical solution was heated to a desired pre-expansion temperature by the heated nozzle and throttled across the expansion unit that consisted of a sapphire capillary nozzle with a diameter of 0.102 mm and a length of 0.254 mm. The nozzle was mounted in a holder with the holder outlet 1 mm in diameter and 1.5 mm thick, coaxial with the holder. The heating of the nozzle was required to avoid nozzle clogging. The conditions of the RESS process used in this work are summarized in Table 1. The position of the Mach disc is expected to be within 1 mm from the nozzle, as follows from the theoretical calculations and experimental measurements for free supersonic expansion of pure supercritical CO_2 using similar nozzles and experimental conditions.[21] Nanoscale particles are formed downstream the jet and measured in the sampling zone of the experimental setup shown in Fig. 1.

In the sampling zone, the particles are illuminated perpendicular to the jet by unpolarized light from two excimer pulse lasers. The delay time between the pulses from the first laser (OPTex eximer laser, Lambda Physik Inc., KrF, wavelength 248 nm, 0.36 mJ $pulse^{-1}$) and the second laser (EX100 eximer laser, Gam Laser Inc., KrF, wavelength 248 nm, 0.24 mJ $pulse^{-1}$) was 0.8 μs (all energies are after the beam forming slit). The energies of the two pulse lasers were measured by a laser energy meter (J50 LP-1, Molectron Detector Inc.). The light scattered by the particles was focused by a fused silica lens (focal length 74 mm at 248 nm) with a 6 mm in diameter aperture to an ICCD camera (ICCD-MAX, Princeton Instruments Inc.). In the initial experiments, a single fused silica lens was used to project images. In the course of the experiments,

Table 1 RESS conditions used in the experiments

Conditions	Pressure/ bar	Saturator temperature/ °C	Nozzle temperature/ °C	Solubility of RDX [3]/ mg RDX g^{-1} CO_2
A	180	80	140	0.035
B	90	60	80	<0.001

this lens was replaced by a fused silica doublet corrected for spherical aberrations with a 15 mm diameter aperture. The distance between the sampling zone and the lens was 92 mm for the single lens and 60 mm for the doublet. The solid angle for the light collection was calculated from the aperture diameter and the distance between the sampling zone and the lens. The optical magnification of the system was 4.1 with the single lens and 3.1 with the doublet. The beams crossing at a small angle (*ca.* 2°) in the vertical plane were passed through a slit 0.9 mm wide and 2.6 mm high. In the observation zone located 30 mm from the slit, the beams were overlapped by 1.3 mm. The dimension of the sampling volume along the beams was determined by the camera field of view and the lens magnification (1.6 mm for the single lens and 2.2 mm for the doublet). The sampling volume was, therefore, almost rectangular parallelepiped with the dimensions 1.3 mm height × 1.6 mm width × 0.9 mm depth in the experiments with two lasers and the single lens. In the experiments employing the doublet, a single laser was used. The slit in this case was 0.55 mm wide and 1.7 mm high, so that the sampling volume was 1.7 mm height × 2.2 mm width × 0.55 mm depth. In the experiments with two lasers, the particles in the sampling zone were illuminated by two consecutive pulses, hence, the ICCD camera recorded two images (''double images'') from each particle. An example of such a frame is shown in Fig. 2. Some particles travel out of or in the sampling zone during the time between the two pulses. A single spot was then observed for such particles. This technique was used to determine the velocity and the direction of the flow in the jet. An example of the axial flow velocity field in the RESS jet at the pre-

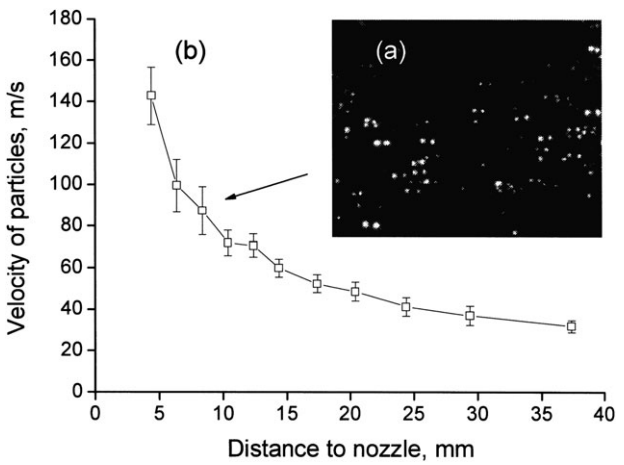

Fig. 2 (a) An example of a frame with double images of particles; (b) axial velocity of particles as a function of the distance from the nozzle along the RESS jet (experimental conditions: set B, Table 1). The arrow shows the point where the frame was taken.

expansion pressure 90 bar determined in this way is shown in Fig. 2.

In the ICCD camera output, the light intensity field is expressed in ''counts'' per pixel. Two calibrations were performed to link the ICCD counts to the scattered light intensity. In the first method Rayleigh scattering from air was used. In the second method scattering from standard polystyrene spheres was used for calibration. To increase the signal from Rayleigh scattering from air, the incident beam was focused by a lens. In these experiments, the slit was removed. For the calibration using standard particles, the standard polystyrene spheres with known mean diameters of 102 ± 3 and 152 ± 5 nm (NANOSPHERE™, Catalog numbers 3100A and 3150A, Duke Scientific Corporation, ± refers to the uncertainty in the mean diameter) were used. According to the manufacturer specifications, the standard deviations of the sphere diameters were 4.4 nm for the 102 nm standard spheres, and 3.2 nm for the 152 nm standard spheres. Original aqueous solution containing 1 wt% of polystyrene particles with small amount of a surfactant was diluted 2000 times by methanol. Then this solution was dispersed using an aerosol generator (ATM 225, Topas GmbH). Additional air flow was admixed downstream the aerosol generator to evaporate methanol droplets and carry airborne latex particles to the observation zone of the experimental setup.

The images captured by the ICCD camera were processed to locate the spots and to determine the spot intensity distribution functions as follows. First, two-dimensional Fourier transform was carried out on each frame to filter out the low frequency background noise. After that, the locations of the spots were searched and the integral intensities of the spots were calculated by summing up the ICCD counts in the pixels composing one spot. Finally, the intensity histograms were obtained by sorting the spot integral intensities into an appropriately binned intensity (or diameter) axes.

Upon traveling in air, the jet was diluted due to air entrainment. The magnitude of the air entrainment in the jet was evaluated based on the temperature measurements as well as the Raman scattering intensities of CO_2 along the jet. The axial temperature profiles of the jet were measured using a K-type thermocouple made of chromel and alumel wires with a diameter of 0.1 mm.

The experimental setup for the Raman measurements was slightly modified compared to the setup shown in Fig. 1. In these experiments the ICCD camera was mounted on a spectrograph. The light scattered in the jet was guided into the spectrograph (SpectraPro-300i, Acton Research Corporation). A laser light rejection filter (UV steep edge filter, Barr Associates, Inc.) which blocks more than 99.99% of light at 248 nm was installed on the entrance slit of the spectrograph. The slit width was 50 μm, which corresponds to the spectral resolution of 1.1 nm.

3. Results and discussion

Some essential terms used in the discussion are explained below.

• ''Counts'' are artificial units for the light intensity used in the output of the ICCD camera. The raw data are presented in

terms of counts per pixel. The sensitivity determined *via* the calibration procedures is used to convert "counts" into the number of incident photons (section 3.1)

• A frame is an image obtained after a single laser shot. Frames can be accumulated by summing up the counts in pixels.

• A bin is an interval on the scattered light intensity (differential scattering cross-section) or on the particle diameter axis. In all cases in this paper, the bin structure used was obtained by dividing of an appropriate axis *evenly in the log scale*. For the scattering light intensity axis (or the differential scattering cross section) the bin system of 20 bins decade^{-1} was used. For the particle size axis, the bin system was 60 bins decade^{-1} (section 3.3). In the Rayleigh scattering region, where the scattering cross section is proportional to d^6, one decade of the particle diameter corresponds to six decades of the scattered light intensity. It means that in the binning system used one bin of the particle size exactly corresponds to two bins in the scattering cross-section. However, in the Mie scattering region, where no power relationship between the scattered light intensity and the particle diameter exists, interconversion of the two bin system is more complicated, as explained in section 3.3.

3.1. Calibration of the sensitivity

A sample image of Rayleigh scattering from air is shown in Fig. 3a. In this image, 30 frames were summed up so that the intensity is 30 times larger than the intensity in a single frame. The white strip is the image of the laser beam produced by the Rayleigh scattering from air. Fig. 3b presents the cross section along the horizontal axis of this image. The sensitivity of the ICCD camera was calculated by dividing the integral intensity (the area below the curve) by the theoretical number of photons collected by the camera. This was done for different

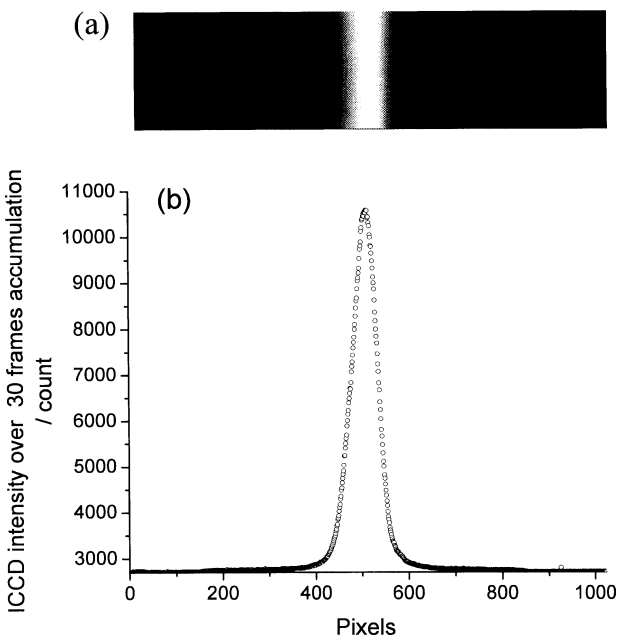

Fig. 3 (a) An image of Rayleigh scattering from air; (b) average cross section of the image.

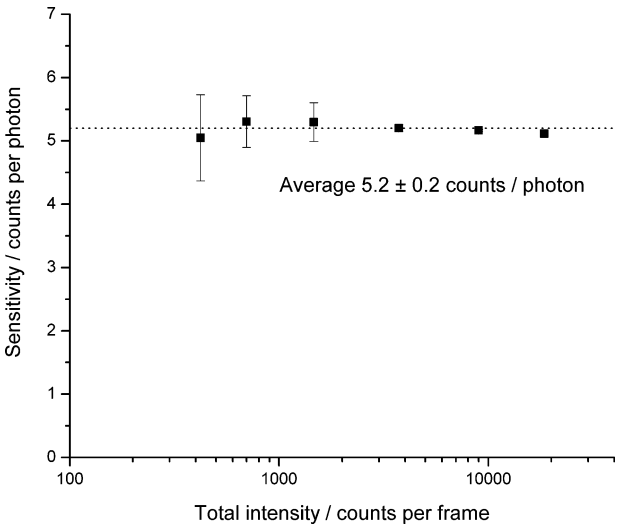

Fig. 4 Sensitivity of the ICCD camera as a function of the total intensity of light collected by the camera. (The error shown is the statistical error only.)

intensities of the incident light, and the dependence of the sensitivity on the light intensity was determined (Fig. 4). The details of the sensitivity determination are described in Appendix A (ESI).† Fig. 4 shows that the sensitivity of the ICCD camera is independent of the incident light intensity. The absolute error of the calibration, mainly determined by the accuracy of the laser energy measurements, is about ±20%. The error in the sensitivity results in ±7% error in the diameter of 100 nm RDX particles and ±5% in the diameter of 70 nm RDX particles.

Fig. 5 shows the measured intensity distribution of the scattered light from standard polystyrene particles of 102 and 152 nm diameter. Two features are apparent in Fig. 5, the difference in the widths of the two distribution functions as well as a "pedestal" on the small particle side of the distribution function for 152 nm particles. The "pedestal" was attributed to

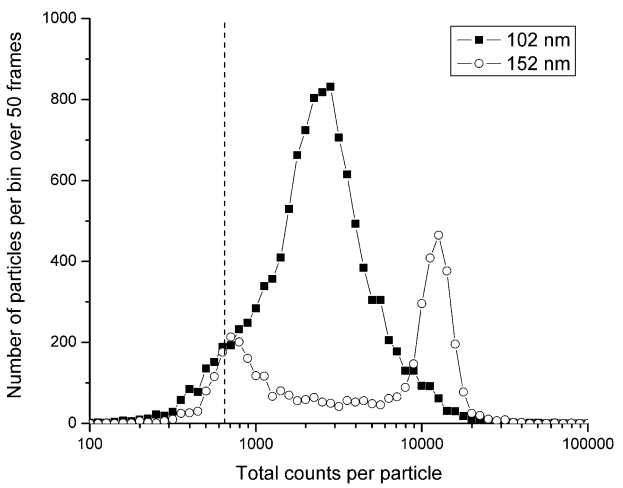

Fig. 5 Distribution functions of the scattered light intensity from standard polystyrene spheres of 102 nm in diameter (filled squares) and 152 nm (open circles). The dashed line represents the cut-off for the small size limit of particle detection.

the particles of the surfactant, which was present in the original solution of the latex particles in the concentration of 0.1 wt%. After 2000 times dilution, the solution is expected to produce particles of the surfactant with an estimated diameter of *ca.* 6 nm, assuming that the aerosol generator used forms droplets of *ca.* 1 μm in diameter. The total concentration of such particles is expected to be *ca.* 200 times larger than the concentration of 102 nm latex particles, and the "pedestal" is due to the large size "tail" of the distribution function for surfactant particles. This could have also a minor impact on the shape of the distribution function for 102 nm particles.

The narrow distribution function obtained for 152 nm particles is consistent with the much weaker dependence of the scattered light intensity on the particle diameter at 152 nm (compared with 102 nm) as follows from the Mie theory. The width of the distribution function for 102 nm particles is consistent with the broadening due to the non-uniformity of the laser light intensity in the sampling volume (±3%), to the fluctuation of the laser pulse energy (±18%), and to somewhat larger standard deviation for the 102 nm latex particles (±6 nm) as indicated in the literature.[22]

The sensitivity was determined based on the differential scattering cross section at 90° for unpolarized light for polystyrene spheres calculated using the Mie theory[20] and the ICCD intensity counts at the maximum of the intensity distributions in Fig. 5. In these calculations, the complex index of refraction of polystyrene at 248 nm was taken as $1.803 + 0.0072i$, as evaluated from the dielectric constants of polystyrene.[23] The Fortran program, Chiral,[24] downloadable from Internet, was used as a Mie scattering code. The sensitivity determined from the calibration using the polystyrene spheres was 5.2 ± 0.6 counts per incident photon, in good agreement with the results of the Rayleigh scattering calibration (5.2 ± 0.2 counts per incident photon). The sensitivity determined in these calibration experiments was used to convert "counts" in a pixel (an artificial unit specific for a given instrument) to the number of incident photons hitting the photocathode of the ICCD camera.

3.2. Distributions of the scattered light intensity from RDX particles formed in the RESS jet

The scattered light intensity distribution functions for two sets of experimental conditions are presented in Fig. 6. The scattered light intensities were converted to the differential scattering cross sections using the ICCD camera absolute sensitivity. In both experimental conditions, the intensities of the spots decreased downstream the jet. There is no other possible explanation for the decrease in the spot intensities other than that the particles initially formed near the nozzle consisted mainly of CO_2, which subsequently evaporated downstream the jet, finally leaving only RDX in the particles.

The intensity distribution functions for the particles formed at the pre-expansion pressure of 180 bar (Fig. 6a) retain similar shape and the same peak intensity after the distance of 59.5 mm from the nozzle, thus all condensed carbon dioxide is expected to evaporate. On the other hand, the distribution functions for the particles formed at the pre-expansion pressure of 90 bar (Fig. 6b) were moving toward the lower intensity until all particles become unobservable. The steep edges in the distribution functions of the particles after 26.5 mm in Fig. 6b are the cutoff boundaries associated with the limit of particle detection. It should also be noted that the limit of the particle detection for the measurement at the pre-expansion pressure of 180 bar was improved as a result of the replacement of the single lens by the doublet lens.

3.3. Size distribution of RDX particles

Fig. 7 shows an example of a SEM image of RDX particles produced in our experiments. To collect the samples for the SEM analysis, the nozzle was oriented to generate the RESS jet horizontally. Glass substrates were placed at the distance of 10 cm from the nozzle and *ca.* 1.2 cm from the jet axis to deposit particles by sedimentation. The image shows individual particles with an almost spherical shape. We estimated the effect of non-sphericity of RDX particles on the scattered light intensity assuming that their shape can be approximated by a spheroid with the aspect ratio 1.2. For the estimates we used a T-matrix method,[25] and considered all possible orientations of the spheroids relative to the incident laser beam. The results are presented in Fig. 8. The complex index of refraction for RDX at 248 nm was taken as $1.678 + 0.645i$ (Appendix B, ESI).† As can be seen from Fig. 8, the differential scattering cross sections averaged over the orientations of the spheroids with the aspect ratio of 1.2 can be approximated as those of a sphere. The error associated with the replacement of the spheroid with a spherical particle of equal volume is insignificant below 100 nm (less than ±5% of the particle size). Above 100 nm the error becomes larger (about a factor of 2). Therefore, the Mie theory for spherical particles gives relatively accurate results for the size distributions of RDX particles below 100 nm, and the size distributions close to the average over random orientations of RDX spheroid particles above 100 nm. Fig. 9 shows the theoretical differential scattering cross sections for spherical particles of solid RDX and CO_2 as functions of particle diameter. The index of refraction for CO_2[26] at 248 nm was taken as $1.475 + 0i$.

The differential scattering cross sections (Fig. 9) were used to convert the intensity distributions (*i.e.*, the distributions of the experimental differential scattering cross section) to the particle size distributions, when the data were outside the oscillating region (the region between the points (d_1, σ_1) and (d_2, σ_2) for RDX particles shown in the zoomed insert in Fig. 9). Using this approach, the size distribution of RDX particles formed at the pre-expansion pressure of 180 bar was determined from the intensity distribution functions measured at 69.5 mm from the nozzle (Fig. 10). In the distribution functions in terms of the scattered light intensity (differential scattering cross section), the intensity scale was evenly binned in the log scale with the spacing of 20 bin decade^{-1}. To convert to the particle size distribution functions, the following procedure was used. The size axis was evenly binned in the log scale with the spacing of 60 bin decade^{-1}. The corresponding boundaries of the bins were converted into the boundaries of the bins in the differential scattering cross section scale based on the Mie theory calculations. Then, the original raw data were reprocessed by re-sorting of the spots intensities with the

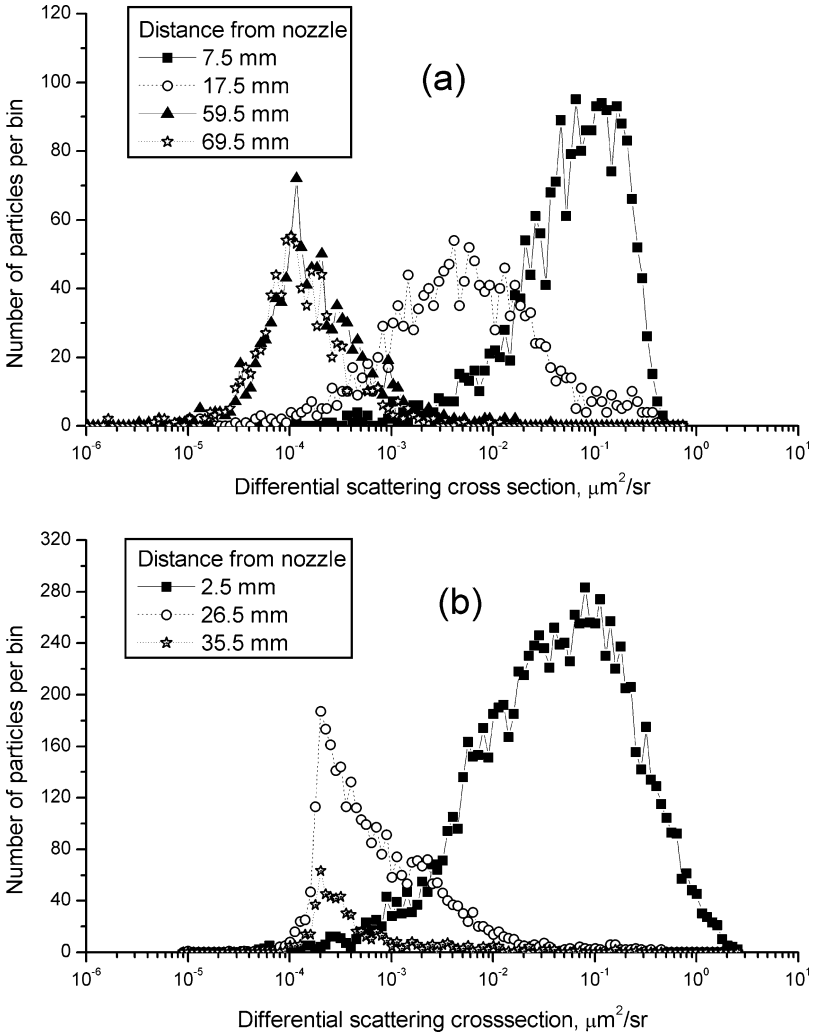

Fig. 6 Intensity distribution functions of the scattered light from particles formed in the RESS jet. (a) Experimental conditions: set A, Table 1. Filled squares – 7.5 mm, open circles – 17.5 mm, filled triangles – 59.5 mm, open stars – 69.5 mm from the nozzle. A doublet corrected for spherical aberrations was used in this experiment. (b) Experimental conditions: set B, Table 1. Filled squares – 2.5 mm, open circles – 26.5 mm, open stars – 35.5 mm from the nozzle. A single lens with small aperture was used in this experiment. The distribution functions are truncated from the lower intensity side at the sensitivity limit of the experiment.

new bin system. The range between the two dotted lines labeled as ''ambiguous region'' in Fig. 10 corresponds to the oscillation range in the differential scattering cross section of RDX particles. Due to the impossibility of unambiguous assignment of the differential scattering cross section to the particle diameter in this region, the shape of the distribution function in this region cannot be determined. However, the total number of particles still can be determined with certainty by summing the number of particles per bin counted between σ_1 and σ_2 in the intensity distribution function. The dashed line in Fig. 10 shows the total number of particles in the ''ambiguous region'' divided by the total number of bins in this region (*i.e.*, the average number of particles per bin). One of the conclusions made from Fig. 10 is that the particle size at the maximum of the distribution is 73 nm, given that even the total number of particles in the ambiguous region is smaller than the maximum value at 73 nm. The particle sizes obtained from the *in situ* measurement are somewhat smaller compared to the typical particle sizes measured using SEM. For example, the mean diameter of RDX particles collected by sedimentation inside a RESS chamber was 150–200 nm as determined by SEM. This discrepancy could be due to the size discrimination when the particles were collected for the SEM analysis. The size distribution of CO_2 particles formed near the nozzle could not be recovered from the optical measurements by the method described above because the oscillations in the differential scattering cross sections of CO_2 particles become much more significant for the large particle sizes (Fig. 9) (the inverse light scattering problem). Therefore, a different approach described below was used.

3.4. The Monte-Carlo approach for modelling an ensemble of particles

Since the inverse Mie scattering problem has non-unique solution in a particular region of diameters, we determined the parameters of the distribution function, assuming a particular shape of the distribution function, namely the log-

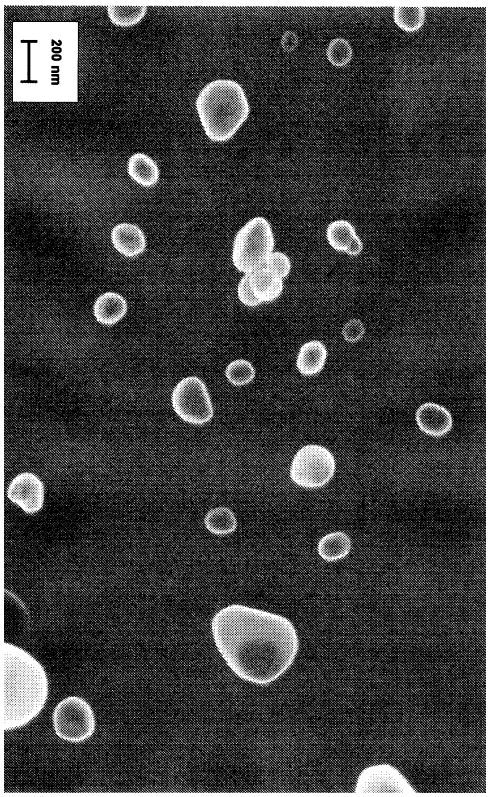

Fig. 7 Sample SEM image of RDX particles obtained by the RESS (set A, Table 1).

normal distribution $L(d)$:

$$L(d) = \frac{A}{\Omega\sqrt{2\pi}}\exp\left(-\frac{(\ln d - \ln \mathrm{M})^2}{2\Omega^2}\right)\left(\frac{1}{d}\right) \qquad (1)$$

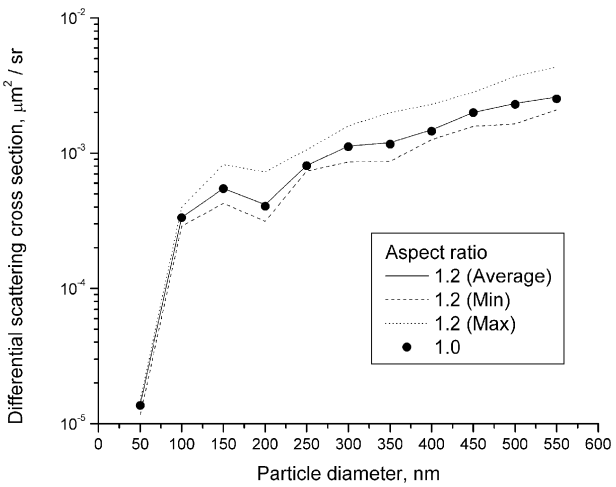

Fig. 8 Light scattering cross section from non-spherical (spheroid) RDX particles at 90° for unpolarized incident light as a function of the equal-volume-sphere diameter. Solid line – the average differential scattering cross sections for all possible orientations of spheroids with the aspect ratio of 1.2. Dashed line – the minimum differential scattering cross sections at the aspect ratio of 1.2. Dotted line – the maximum differential scattering cross sections at the aspect ratio of 1.2. Filled circles – the differential scattering cross sections of spheres (aspect ratio of 1.0).

where M and Ω are the parameters of the log-normal distribution, A is the area below the curve, and d is the particle diameter. An ensemble of particles was modeled using the Monte-Carlo approach.[27] In this approach, the precision is not limited by the number and the size of the bins in the histograms. The theoretical statistical error can be easily estimated by simulating several independent random ensembles and compared with the statistical error of the experimental data obtained by repeated experiments.

The Monte-Carlo approach was implemented as follows. An ensemble of 10^5 particles with the same refractive index and random diameters was simulated using a uniform random number generator. Then, for given values of M and Ω, eqn (1) was used to assign statistical weight to each particle. This statistical weight was taken into account when building the distribution of the particles with respect to their differential scattering cross sections. Varying the values of M and Ω and using the Levenberg–Marquardt non-linear least squares fitting algorithm,[28] the best fit to the experimental data was performed.

3.5. Size distributions determined using the Monte-Carlo approach

The theoretical distributions of a differential scattering cross section of particles determined using the Monte-Carlo approach were compared with the experimental data from the measurements near the nozzle (7.5 mm from the nozzle) and far from the nozzle (69.5 mm from the nozzle) (Fig. 11). The tails of the experimental distribution function obtained near the nozzle as well as far from the nozzle could not be fitted by the models produced by the Monte-Carlo simulations. It means that the true particle size distributions were not exactly log-normal distributions. Nevertheless, as the particle sizes at the maximums of the distributions were still valid, we estimated that the particle size consisting of CO_2 with a small amount of RDX at the maximum in the distribution was 3.3 μm in diameter at 180 bar RESS pre-expansion pressure and the RDX particle size at the maximum was 73 nm (Fig. 12). The particle size in the maximum determined using the Monte-Carlo approach was exactly the same as that determined using the direct method in Fig. 10.

Reference experiments were performed with no RDX dissolved in the supercritical carbon dioxide at the otherwise identical experimental conditions. It was observed, that dissolution of RDX has significant impact both on the scattering images and the temperature profiles. When RDX was present in the solution, large particles were formed much earlier. The temperature at the same position in the jet was substantially higher (*e.g.*, by 35 K at 7.5 mm from the nozzle). These observations imply that the solute (RDX) has direct impact on the nucleation rate. Earlier nucleation accelerates earlier particle growth, which leads to enhanced heat release. This, in turn, explains the difference in the observed temperature profiles.

3.6. The number density of particles in the RESS jet

The number densities of particles were determined by dividing the number of particles per frame by the sampling volume of

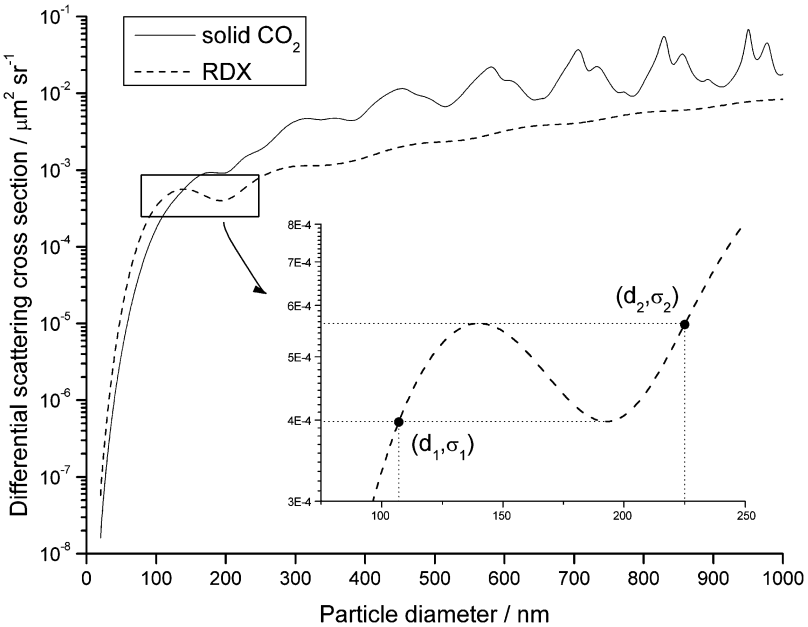

Fig. 9 Differential scattering cross sections from spherical particles of solid CO_2 (solid line) and RDX (dashed line) at 90° for unpolarized incident light as a function of the particle diameter less than 1000 nm. Insert: enlarged region where unambiguous assignment of the particle diameter based on the scattered light intensity is not possible (''ambiguous'' three-valued region).

the laser light scattering. Near the nozzle, the spot counting software underestimated the number of particles (due to the partial overlap of the spots) as compared to manual counting. The correction factor as a function of the distance along the jet was introduced to correct for this effect. The number densities for the RESS at 180 bar and 90 bar pre-expansion pressures were given in Fig. 13. In both cases the observed number densities decreased rapidly downstream the jet. This could be partially or completely due to the air entrainment into the jet. For the 180 bar pre-expansion pressure the apparent number densities were still measurable after 40 mm distance from the nozzle, while for the 90 bar the number density became close to zero. The reason for this could be that the particles produced in the RESS at 90 bar pre-expansion pressure are too small to be detected, as could also be expected from the intensity distribution at the 35.5 mm distance from the nozzle in Fig. 6b.

The impact of air entrainment was evaluated using the mole fraction of CO_2 in the jet determined based on the jet temperature measurements and the Raman scattering spectroscopy. Raman scattering is a proven convenient technique for

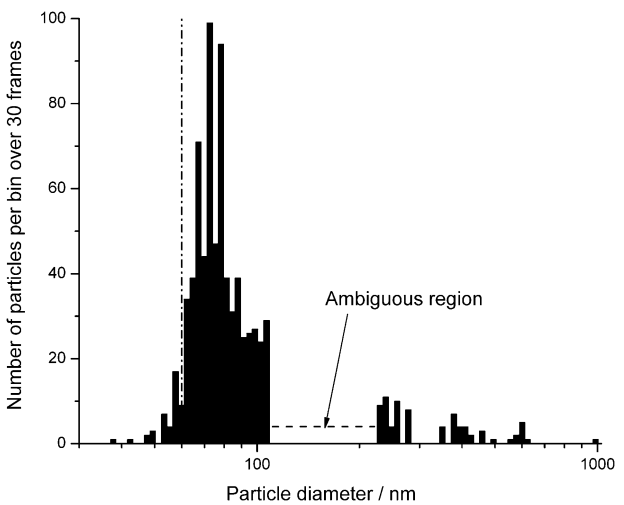

Fig. 10 The size distribution of RDX particles at 69.5 mm from the nozzle. The dashed line represents the averaged number of particles per bin in the ''ambiguous region'' (see text for details). Set A, Table 1.

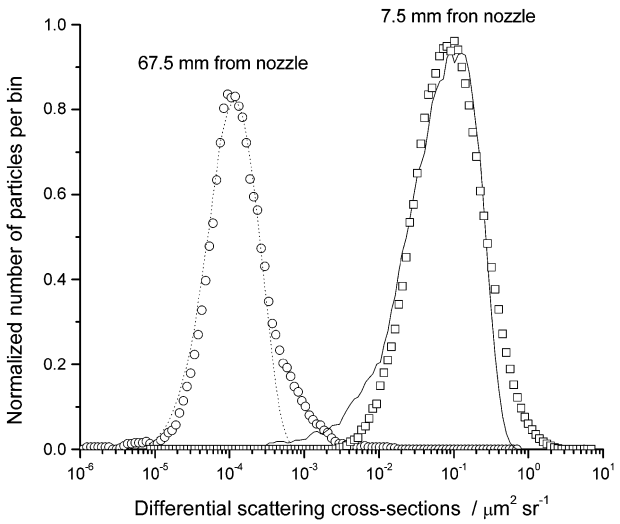

Fig. 11 Comparison of the experimental distributions of the differential scattering cross sections with the log-normal distributions obtained using the Monte-Carlo approach. Open squares: the experimental data, solid line is the log-normal fit to the experimental data at a distance of 7.5 mm from the nozzle. Open circles: the experimental data, dotted line is the log-normal fitting curve at a distance of 69.5 mm from the nozzle.

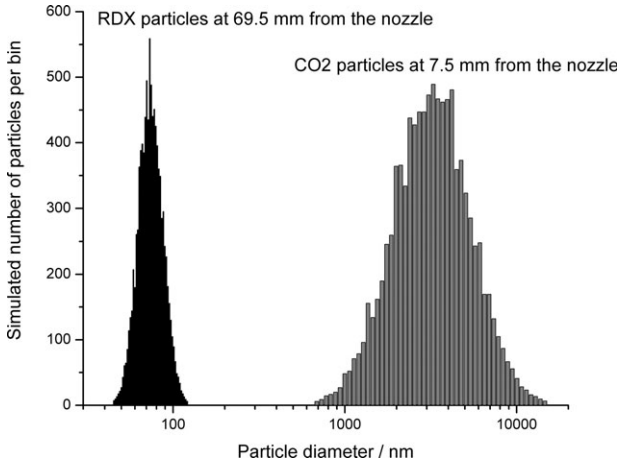

Fig. 12 The particle size distributions determined using the Monte-Carlo approach for CO_2 particles at a distance of 7.5 mm from the nozzle (a) and RDX particles at a distance of 69.5 mm from the nozzle (b).

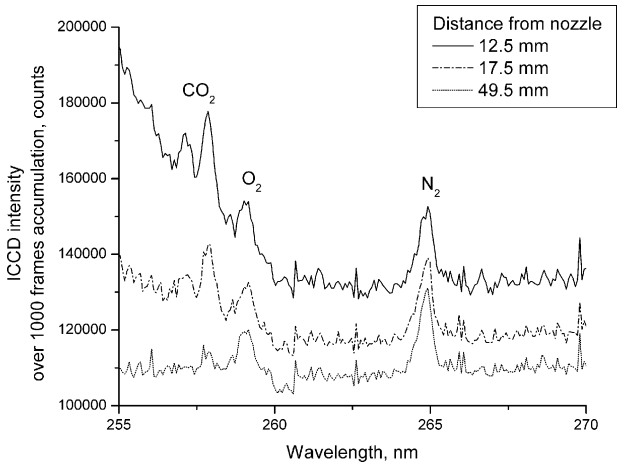

Fig. 14 Raman spectra at the different positions from the nozzle. Solid line – 12.5 mm, dash-dotted line – 17.5 mm, and dotted line – 49.5 mm from the nozzle.

investigation of supersonic jets.[29] Fig. 13 shows the temperature rise downstream the RESS jets at 180 bar and 90 bar pre-expansion pressures. Assuming atmospheric pressure in the jet and the temperature rise only due to the air entrainment, the mole fraction of CO_2 was calculated as:

$$x_{CO_2} = \frac{T_0 - T(z)}{T_0 - T_i - 0.160(T - T_i) + 1.40 \times 10^{-3}(T^2 - T_i^2)} \quad (2)$$

where T_0, T_i, and $T(z)$ are the temperature of surrounding air, the initial temperature, and temperature of the jet at the axial point z, respectively (Appendix C, ESI).† The initial temperature was estimated by extrapolating the temperature profile with a polynomial function. Taking into account the volume change due to the temperature rise by the ratio of T_i to $T(z)$, the number density of particles corrected for the air entrainment is given by

$$n_{cor}(z) = \frac{n(z)}{x_{CO_2}}\left(\frac{T(z)}{T_i}\right) \quad (3)$$

where $n(z)$ is the observed number density.

The Raman spectra of CO_2 and air (Q-branches) at different location downstream the RESS jet are shown in Fig. 14. The Raman shifts for CO_2 are 1388 and 1285 cm^{-1}, which correspond to the vibration mode of C–O symmetric stretching split by the Fermi resonance.[30] Even when using the laser line cut-off filter, there still was a "tail" from the combined light scattering by the turbulent flow, and Rayleigh and Mie scattering from the gas molecules and particles, especially at short distances from the nozzle (Fig. 12). These tails were taken into account in the spectra fitting. The contribution of the condensed carbon dioxide in the Raman peak was estimated not to exceed 1% even in the closest point to the nozzle (7.5 mm); this contribution was neglected. The mole fraction of CO_2 is:

$$x_{CO_2} = \frac{I^{Raman}(z)}{I_0^{Raman}}\left(\frac{T(z)}{T_0}\right) \quad (4)$$

where $I^{Raman}(z)$ and $I_0{}^{Raman}$ are the intensities of Raman peaks of CO_2 at the axial point z along the jet and in pure CO_2 at room temperature T_0, respectively. Eqn (4) also incorporates the temperature correction factor for the number density based on the ideal gas law. The temperature dependence of the differential Raman scattering cross sections in the Q-branch in the temperature range of these experiments was neglected.

Fig. 15 shows the mole fractions of CO_2 along the RESS jet at 180 bar pre-expansion pressure calculated from eqns (2) and (4), the profile based on the Raman data being more reliable. The results of the Raman measurements support the assumption that the temperature rise in the jet is due mainly to the dilution of CO_2 by air entrainment downstream the jet. It was also found that the corrected number densities calculated from eqn (3) do not change along the RESS jet, as shown in Fig. 15.

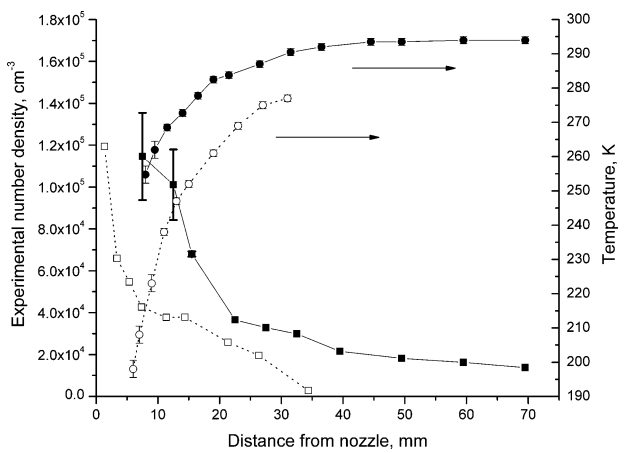

Fig. 13 The number density of particles and the temperature profiles as functions of the distance from the nozzle along the jet. Filled squares and filled circles – set A, Table 1. Open squares and open circles – set B, Table 1.

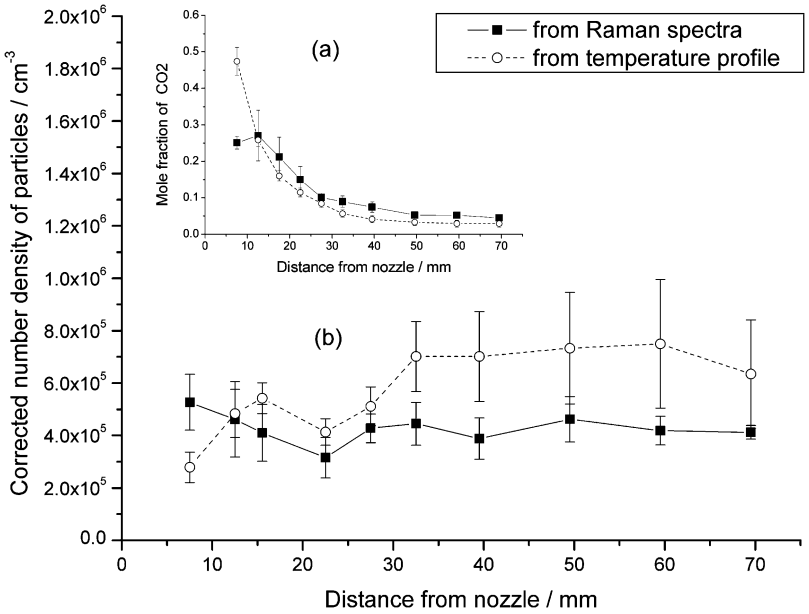

Fig. 15 (a) The molar fraction of CO_2 and (b) the corrected number density of particles as a function of distance from the nozzle along the RESS jet at pre-expansion pressure 180 bar. Filled squares – the data determined from Raman scattering measurements. Open circles – the data determined from the temperature profile of the jet.

We conclude that there is no noticeable particle coagulation occurring in the region investigated and the decrease of the apparent number density along the stream is due to the air entrainment.

3.7. Mechanism of particle formation in RESS

The homogeneous nucleation mechanism is generally invoked to explain nanoparticle formation in the RESS process.[7] In the current research, formation of carbon dioxide particles with their subsequent evaporation was unambiguously observed. Moreover, the particle size experimentally observed *in situ* in the RESS jet is substantially larger than that predicted by the homogeneous nucleation modeled under the most extreme assumptions.

To evaluate the particle size theoretically and to predict the size distribution functions, a numerical kinetic model[31] was used. The model includes all possible processes associated with particle formation (monomer–monomer, monomer–cluster, cluster–cluster) as well as reverse reactions of monomers and clusters evaporation.

Because of very high initial supersaturations in our experiments ($>10^7$), the model is essentially reduced to a set of irreversible processes of particle formation and growth. Under the most extreme assumptions that result in the maximum possible particle size (such as that all processes are irreversible and have gas kinetic cross sections), the model predicts particles of about 5.3 nm in diameter at the pre-expansion pressure of 180 bar at 0.5 ms (as estimated based on the velocity profile in the jet). The predicted size distribution was very close to the so called ''self-preserving size distribution'', tabulated, *e.g.*, by Vemury *et al.*[32] The calculations predict for the time dependence of the mean size $\langle d \rangle \propto t^{2/5}$ in accordance with the scaling theory[33] of agglomerate growth. Therefore, the experimentally observed size of 73 nm would require the duration of the particle growth process $(72/5.3)^{5/2} = 680$ times longer than the time that was experimentally available (0.5 ms). It should be noted that this estimate is based solely on the initial concentration of RDX in the supersaturated solution and does not involve surface tension of RDX or other parameters. It should also be stressed that 5.3 nm for the particle diameter is the maximum theoretically possible particle size predicted by the homogeneous nucleation model.

Therefore, an alternative mechanism, which is a modification of the spray-drying mechanism, is tentatively suggested. The estimates below show the feasibility of such a mechanism. An RDX particle of 73 nm in diameter has 2×10^{-18} moles of RDX assuming the density of RDX particles to be equal to the density of bulk RDX, 1.8 g cm^{-3}. Therefore, a CO_2 particle of 3.3 μm diameter near the nozzle (7.5 mm from the nozzle) is expected to contain 2×10^{-18} moles of RDX (assuming that a single RDX particle is produced from a single CO_2 particle). On the other hand, there are 6×10^{-13} moles of CO_2 in a single CO_2 particle of 3.3 μm diameter, if CO_2 particles are assumed to be solid with the density of 1.4 g cm^{-3}. Then the mole fraction of RDX in CO_2 in a 3.3 μm CO_2 particle is *ca.* 3×10^{-6}. The mole fraction of RDX in the saturated supercritical solution calculated from the solubility of RDX in supercritical CO_2 (Table 1) is 7×10^{-6}, which agrees with the above estimate within a factor of three.

Tentatively, the suggested mechanism is as follows. Initially, under expansion, CO_2 particles are formed. RDX molecules serve as nucleation centers. Subsequently, carbon dioxide condenses entrapping dissolved RDX according to the mole fraction in the supercritical solution. In other words, RDX molecules which were within CO_2 volume to be condensed are entrapped in the formed particles. Therefore, the mole fraction of RDX in the particle reflects the mole fraction of RDX in the

supercritical solution. Upon subsequent evaporation of CO_2, RDX particles are formed. Essentially, this model is the spray-drying mechanism[34] in which solution in a liquid solvent is replaced with a supercritical solution. According to this model, under the conditions with lower solubility of RDX in supercritical CO_2, smaller particles are expected. This is consistent with the inability to detect the final particles in the RESS at the pre-expansion pressure of 90 bar, presumably due to the much smaller particle size below the sensitivity limits of the equipment.

4. Conclusions

In this study, a new experimental approach for the *in situ* monitoring of nanoparticles formed during the rapid expansion of supercritical solutions is developed. The particle size distribution functions were determined *in situ* based on the scattered intensity distribution functions. The examination of the scattered intensity distribution functions revealed the decrease in the particle size downstream the jet. This observation is explained as being due to the evaporation of condensed CO_2. The sizes of RDX particles at the maximum of the distribution functions were smaller than the particle size determined by the SEM analysis, which indicates the size discrimination in the sampling procedure used for the SEM analysis.

The number densities of the particles formed in the RESS jet determined *in situ* by the scattering method were corrected for air entrainment. After corrections the number densities were found to be constant along the jet within the experimental error. Based on these results and the observation on the decrease of the particle size along the stream, a conclusion is made that there is no noticeable particle formation and growth in the jet associated with coagulation of RDX particles.

The experimental data on the particle size and the number density along the jet support the concept of spray-drying-like formation mechanism for RDX particles from saturated supercritical CO_2 solution. The estimated mole fraction of RDX in CO_2 is consistent with the solubility of RDX in supercritical CO_2.

Acknowledgements

This work was supported by the US Army ARDEC under contract number DAAE30-02-C-1140.

References

1 U. Teipel, *Propellants, Explos., Pyrotech.*, 1999, **24**, 134–139.
2 U. Teipel, H. Krober and H. H. Krause, *Propellants, Explos., Pyrotech.*, 2001, **26**, 168–173.
3 V. Stepanov, L. N. Krasnoperov, I. B. Elkina and X. Zhang, *Propellants, Explos., Pyrotech.*, 2005, **30**, 178–183.
4 R. W. Armstrong, C. S. Coffey, V. F. DeVost and W. L. Elban, *J. Appl. Phys.*, 1990, **68**, 979–984.
5 J. Jung and M. Perrut, *J. Supercrit. Fluids*, 2001, **20**, 179–219.
6 K. Vasukumar and A. K. Bansal, *Curr. Res. Inf. Pharm. Sci.*, 2003, **4**, 8–12.
7 P. G. Debenedetti, *Am. Inst. Chem. Eng. J.*, 1990, **36**, 1289–1298.
8 B. Helfgen, M. Türk and K. Schaber, *J. Supercrit. Fluids*, 2003, **26**, 225–242.
9 X. Kwauk and P. G. Debenedetti, *J. Aerosol Sci.*, 1993, **24**, 445–469.
10 R. S. Mohamed, P. G. Debenedetti and R. K. Prude'homme, *Am. Inst. Chem. Eng. J.*, 1989, **35**, 325–328.
11 G. R. Shaub, J. F. Brennecke and M. J. McCready, *J. Supercrit. Fluids*, 1995, **8**, 318–328.
12 J. W. Tom and P. G. Debenedetti, *J. Aerosol Sci.*, 1991, **22**, 555–584.
13 M. Türk, *J. Supercrit. Fluids*, 2000, **18**, 169–184.
14 M. Weber, L. M. Russell and P. G. Debenedetti, *J. Supercrit. Fluids*, 2002, **23**, 65–80.
15 B. Helfgen, P. Hils, C. Holzknecht, M. Türk and K. Schaber, *J. Aerosol Sci.*, 2001, **32**, 295–319.
16 A. Bonnamy, D. Hermsdorf, R. Ueberschaer and R. Signorell, *Rev. Sci. Instrum.*, 2005, **76**, 53904–53908.
17 J. Huang and T. Moriyoshi, *J. Supercrit. Fluids*, 2006, **37**, 292–297.
18 K. Oum, J. J. Harrison, C. Lee, D. A. Wild, K. Luther and T. Lenzer, *Phys. Chem. Chem. Phys.*, 2003, **5**, 5467–5471.
19 D. Hermsdorf, A. Bonnamy, M. A. Suhm and R. Signorell, *Phys. Chem. Chem. Phys.*, 2004, **6**, 4652–4657.
20 C. F. Bohren and D. R. Huffman, *Absorption and Scattering of Light by Small Particles*, Wiley-Interscience, New York, 1988.
21 I. Khalil and D. R. Miller, *AIChE J.*, 2004, **50**, 2697–2704.
22 C.-Y. Wang, S.-P. Pan, G.-S. Peng and J.-H. Tsai, *Proc. SPIE*, 2005, **5879**, 323–328.
23 T. Inagaki, E. T. Arakawa, R. N. Hamm and M. W. Williams, *Phys. Rev. B*, 1977, **15**, 3243–3253.
24 T. Wriedt, http://www.iwt-bremen.de/vt/laser/wriedt/index_ns.html.
25 M. I. Mishchenko and L. D. Travis, *Opt. Commun.*, 1994, **109**, 16–21.
26 S. G. Warren, *Appl. Opt.*, 1986, **25**, 2650–2674.
27 J. M. Hammersley and D. C. Handscomb, *Monte Carlo Methods*, Wiley, New York, 1964.
28 D. M. Bates and D. G. Watts, *Nonlinear regression analysis and its applications*, Wiley, New York, 1988.
29 A. Ramos, J. M. Fernández, G. Tejeda and S. Montero, *Phys. Rev. A*, 2005, **72**, 053204.1–053204.7.
30 T. Shimanouchi, *Tables of Molecular Vibrational Frequencies Consolidated Volume I*, National Bureau of Standards, 1972, pp. 1–160.
31 E. N. Chesnokov and L. N. Krasnoperov, *J. Chem. Phys.*, 2007, **126**, 144504.1–144504.15.
32 S. Vemury and S. E. Pratsinis, *J. Aerosol Sci.*, 1995, **26**, 175–185.
33 M. K. Wu and S. K. Friedlander, *J. Aerosol Sci.*, 1993, **24**, 273–282.
34 K. Masters, *Spray drying: an introduction to principles, operational practice, and applications*, Wiley, New York, 1976.